Experiments in Fluids manuscript No.
(will be inserted by the editor)

Designing a maximum precision interferometric particle imaging set-up

S. Dehaeck[1,2], **J.P.A.J. van Beeck**[1]

[1] Von Karman Institute for Fluid Dynamics, Waterloose Steenweg 72, B-1640 Sint-Genesius-Rode, Belgium

[2] Dept. of Flow, Heat and Combustion Mechanics, Ghent University, St.-Pietersnieuwstraat 41, B-9000 Gent, Belgium

The date of receipt and acceptance will be inserted by the editor

Key words ILIDS, IPI, MSI, GSI, Glare Points, Droplets, Bubbles, Metrology

Abstract In this article, a comprehensive uncertainty analysis will be given of a popular 2D particle measuring technique called Interferometric Laser Imaging for Droplet Sizing (ILIDS). This includes the first estimates on the influence of droplet non-sphericity. Next to this, the uncertainty on the frequency determination and the calibration procedures were also investigated. To this end, the two most common calibration procedures were experimentally compared. This showed that it often dominates the total uncertainty. Design guidelines are then derived concerning observation angle, out-focus disk size and calibration procedure which could lead to a combined uncertainty below 1.5%.

1 Introduction

Interferometric laser imaging for droplet sizing (ILIDS), as introduced by Koenig et al. (1986), Ragucci et al. (1990) and Glover et al. (1995), is a popular technique for measuring droplet and bubble size in a 2D plane. This technique is also known under various different names as IPI (Interferometric Particle Imaging) and MSI (Mie Scattering Imaging). In this technique, translucent particles are illuminated by a laser-sheet. Depending on the observation angle, one or multiple bright points (i.e. glare points) are visible on the particle surface. The distance between any two of these glare points can be used to calculate the particle size (Hess (1998); Dehaeck et al. (2005)). When these points are imaged out-focus, an interference pattern will become visible with a shape that is determined by the aperture. The angular frequency of this pattern is proportional to the separating distance between the two glare points and thus to the particle diameter.

Correspondence to: sam.dehaeck@gmail.com

In spite of the literature available, there is to date no real consensus on the best configuration. For the most studied case of measuring droplets, there are roughly 5 different configurations possible; with perpendicular polarized light, researchers have measured at an observation angle of 35° (Koenig et al. (1986)), at 60° (Massoli and Calabria (1999)) and at 68° (Burke et al. (2002)). But also measurements with parallel polarization at 90° (Damaschke et al. (2002a)) and with circular polarization at 73° (Maeda et al. (2000)) have been performed. In section 3, the connection between the uncertainty of the measurements and the chosen observation angle will be shown. In addition, a first quantification of the impact of droplet non-sphericity on the diameter estimation will be given in this section.

When faced with the problem of choosing the appropriate set-up for a particular problem, the article of Damaschke et al. (2002b) already gives several tips. They clearly explain how the choice of the distance between the camera and the laser-sheet influences the attainable concentration limit. However, this article did not discuss the choice of an observation angle, nor did it discuss the implications of choosing smaller out-focus disk sizes on the overall precision of the measurements. In section 4, the uncertainty on the frequency determination will be derived analytically. From this derivation, we will show how the theoretical configurations proposed by Damaschke et al. (2002b) to obtain the highest possible concentrations, lead to uncertainties of up to 4%!

Section 5 will deal with the different calibration procedures available for ILIDS. Again, no systematic comparison is available in literature, nor any estimation of the associated uncertainty. An experimental comparison of the two most prominent calibration techniques has been performed. This has revealed the strengths and weaknesses of both approaches.

Finally, an integrated view of the different design constraints and calibration procedures will be given in the discussion.

2 ILIDS Formula

For ILIDS, the particle diameter D is derived as follows (Semidetnov and Tropea (2004) and Dehaeck and van Beeck (2006)) :

$$D = \frac{\lambda \alpha_{air}}{\Delta \varphi_{air}} \tag{1}$$

Here, λ is the wavelength, $\Delta\varphi_{air}$ is the fringe spacing in air (in radian) and α_{air} is the conversion factor to calculate the particle diameter from the observed glare point separation in air as used in GPVS (Dehaeck et al.

(2004)). Note that the advantage of this representation is that all implementation specific knowledge is stored in the factor α_{air}. This implies that the only difference when working with bubbles as opposed to droplets will be visible in the different numerical value of α_{air}. This allows for an easy separation of uncertainty sources that are common for all ILIDS implementations and those sources that are implementation specific. Now, while α_{air} can be calculated from the optical configuration, the fringe spacing $\Delta\varphi_{air}$ has to be extracted *in radian* from the ILIDS images. This is not straightforward however and there are different approaches to achieve this. Most current techniques separate this in two sub-tasks; a) measure the fringe spacing in pixels F_{pix} with a Fast Fourier Transform and b) multiply this value with a 'calibration' value $C_{pix/rad}$ to convert this from pixels to radian.

$$D = \lambda \alpha_{air} F_{pix} C_{pix/rad} \tag{2}$$

As the uncertainty related to the laser wavelength is negligible compared to the other sources, only the uncertainty related to the three remaining parameters are taken into account:

$$\frac{\Delta D}{D} = \sqrt{\left(\frac{\Delta \alpha_{air}}{\alpha_{air}}\right)^2 + \left(\frac{\Delta F_{pix}}{F_{pix}}\right)^2 + \left(\frac{\Delta C_{pix/rad}}{C_{pix/rad}}\right)^2} \tag{3}$$

Each of these uncertainty sources will be discussed in detail in the following three sections. In the discussion, an integrated view will be offered of how these error sources can be minimized by choosing appropriate set-up parameters.

3 Uncertainty analysis of the conversion factor α_{air}

3.1 Introduction

The conversion factor α_{air} depends on the used glare points, the observation angle θ, the relative refractive index n_{rel} and the non-sphericity of the particle. The sensitivity of α_{air} to these variables has already been extensively studied for bubble measurements in Dehaeck et al. (2005). For measurements of droplets, such a study has been absent so far, in particular the sensitivity to non-sphericity is unknown. Therefore, only the case of measuring droplets from the interference pattern created by externally reflected light and refracted light will be discussed here.

The presented study is based on numerical results obtained from a 2D ray-tracing program. As has been proven several times in literature, such calculations differ by less than 1% from rigorous calculations performed with the

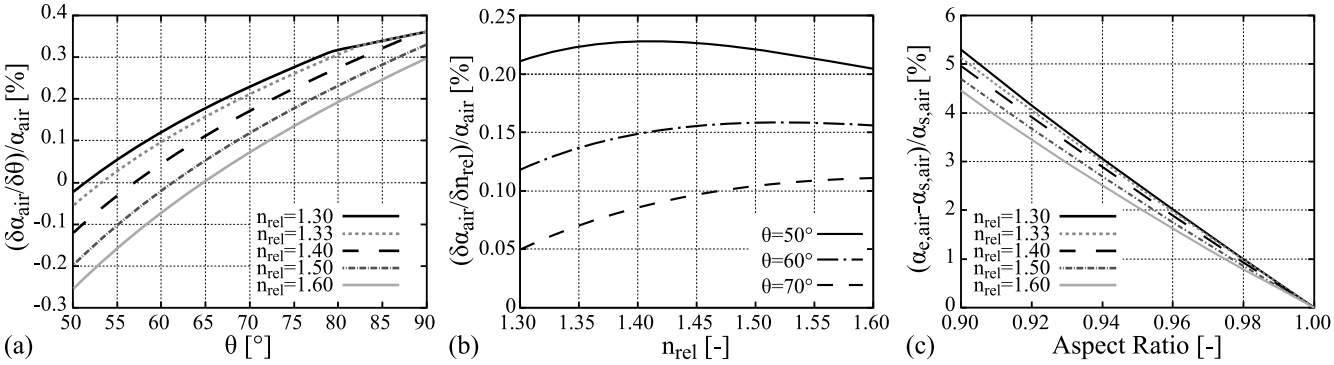

Figure 1 Relative uncertainties in the conversion factor α_{air} for an uncertainty (a) of 1° in observation angle, (b) of 0.01 in relative refractive index and (c) of deviations from sphericity at an observation angle of 60°

full Lorenz-Mie calculations provided that the particles are roughly larger than 5 μm (e.g. Semidetnov and Tropea (2004); Grassmann and Peters (2004)). However, in our program there are no surface waves. This implies that the results are only valid up to an angle of 82° for water droplets, which obviously excludes measurements under 90°. In order to present results for these angles as well, the analytical formula from Semidetnov and Tropea (2004) was used to extend the results beyond the limit of classical geometrical optics. With θ being the observation angle, adapting this formula to our notation results in:

$$\alpha_{air} = \frac{2}{1 + \cos(\theta/2)} \tag{4}$$

This formula was of course only used to measure spherical particles, it is questionable whether surface waves are visible for ellipsoidal particles.

3.2 Uncertainty of ILIDS configurations for measuring droplets

In figure 1(a), the uncertainty connected to small errors in the observation angle is depicted for measuring droplets with different relative refractive indices. This graph shows the derivative of the α_{air} versus θ curve, non-dimensionalised with the local value of α_{air}. As a result, the procentual error of α_{air} for a misalignment error of 1° is obtained versus the 'intended' observation angle. However, these small differences in observation angle are not necessarily due to a misalignment, the observation angle also changes gradually over the field of view of the camera. Fortunately, the resulting errors are very small (<0.4%) for all considered observation angles. However, note that each curve crosses the x-axis. This crossing point corresponds to a local minimum in the α_{air} versus θ curve. At this angle, no error is made for small changes in the observation angle across the field of view and as such, this angle is a good candidate for measuring droplets.

Figure 1(b) shows the derivative of the α_{air} versus n_{rel} curve non-dimensionalised with the local α_{air} value. This is given for several observation angles. Thus, the y-value gives the procentual error for an uncertainty of 0.01 in the relative refractive index. As noticeable on this graph, using larger observation angles, decreases the sensitivity to the relative refractive index. This is clearly contradicting the results of Massoli and Calabria (1999), where it was stated that the lowest sensitivity to refractive index changes is obtained under 60°. Our results show that measuring under 70° already divides this sensitivity roughly in two. Complete independence of the relative refractive index is obtained when the observation angle is larger than the limiting angle for refraction: $\theta > 2\arccos(1/n_{rel})$. Above this angle, the surface wave creates a glare point at the outer edge of the droplet and its position is thus independent of the refractive index. This is also visible in formula 4. In applications with large variations in refractive index, measuring at angles close to or slightly above the limiting angle is thus advised (if possible).

Finally, figure 1(c) shows the maximum error that can be made when assuming that an ellipse with the given aspect ratio is a sphere when measuring at an observation angle of 60°. This curve was obtained as follows. For any point on this curve, rays were numerically traced through an ellipsoidal droplet with a given aspect ratio and tilt angle (angle between incoming ray and largest axis of the ellipse). The orthogonal distance between those rays exiting the droplet at the prescribed observation angle was calculated. By comparing this distance with the spherical equivalent diameter of the ellipse, the 'ellipsoidal' conversion factor $\alpha_{e,air}$ can be calculated. Since this value depends strongly on the tilt angle, only the maximum $\alpha_{e,air}$ is kept from a loop over all possible tilt angles. Finally, the value in the curve is the procentual error that is made when using the 'spherical' conversion factor $\alpha_{s,air}$ instead of the real ellipsoidal conversion factor. As one can see, this error reaches 5% for water droplets in air when the aspect ratio equals 0.9. Larger refractive indices lower this error somewhat. Although not shown here, these calculations were also performed for different observation angles (but not those angles where surface waves are important). This showed that there is no substantial difference in the error made, implying that there is no optimal configuration to minimize the error due to non-sphericity effects. The curve shown here indicates the maximum over-estimation of the spherical equivalent diameter for any possible tilt angle. However, for a different tilt angle an under-estimation is obtained that is equal in size to the over-estimation. Therefore, the 'average' error was also calculated when an ellipsoid with a given aspect ratio would be measured with all possible tilt angles. This average error is almost negligible and a total overprediction of 0.2% was obtained for a non-sphericity of 0.9 in water. For different refractive indices equivalent results were obtained. This leads to the important conclusion that

measurements of mean particle size remain reliable, even in the presence of moderately non-spherical particles. However, the presence of symmetrical over- and under-estimation will broaden the obtained diameter distribution.

4 Uncertainty analysis of the fringe frequency determination F_{pix}

Since the conversion factor α_{air} contains all the information on the used glare points, the relative refractive index and the observation angle, the following sections will describe 'universal' uncertainties valid for any ILIDS configuration. In this section, the uncertainty related to the estimation of the fringe spacing from the out-focus disks will be discussed. Now, in order to measure the fringe spacing in pixel, a simple periodogram is calculated from the intensity profile with the use of the FFT. From this, one generally uses some form of interpolation to obtain the frequency peak location with a sub-pixel accuracy. Often, a Gaussian interpolation is used but this can also be performed without assumptions concerning the peak profile by zero-padding the signal with a large amount of zeros, followed by a Golden section estimation. Maeda et al. (2000) mentions an adjusted Gaussian interpolation that reduces the bias error to less than 0.3% of the fundamental frequency. However, this does not include the random error that is made by the periodogram due to the presence of noise in the signal. In order to obtain an estimate of this error, the Cramer-Rao Lower Bound (CRLB) needs to be calculated. This is the absolute minimum variation on the estimated frequency that an unbiased estimator can obtain in the presence of white Gaussian noise. The amount of noise present is generally denoted by the signal to noise ratio (SNR); i.e. the power of signal fluctuations σ_s^2 divided by the power of noise fluctuations σ_n^2. More information on estimating the SNR from experiments, the CRLB and its application in laser doppler systems can be found in Albrecht et al. (2003). The periodogram is able to obtain this minimum variation for an SNR larger than -2dB (So and Chan (2005)). Thus, the theoretical error estimate that will be presented now can be understood to come from the periodogram above this threshold. Following Albrecht et al. (2003), the CRLB for frequency estimation in a noisy signal is:

$$Var_{F_{pix}} = \frac{3 f_s^2}{\pi^2 N \left(N^2 - 1\right) SNR} \tag{5}$$

where $Var_{F_{pix}}$ is the variance on the frequency estimate, f_s is the sampling frequency and N is the amount of samples. Applied to this case, a sampling frequency of 1 is used and N equals the amount of pixels present in the ILIDS out-focus disk Φ_{pix}; i.e. $f_s = 1$ and $N = \Phi_{pix}$ =>

$$Var_{F_{pix}} = \frac{3}{\pi^2 \Phi_{pix}^3 SNR} \tag{6}$$

In this formula, a small simplification has been made by setting $\Phi_{pix}^2 - 1$ equal to Φ_{pix}^2, which leads to an error of 0.1% for a diameter of 12 pixels but decreases fast for larger diameters. Now, in order to transform this variance to a procentual uncertainty, the double of the square root of the variance (95% confidence interval) needs to be divided by F_{pix}. This frequency can be expressed in design parameters by noting that the amount of visible fringes N_f is fully determined by the fringe spacing and the collecting angle γ:

$$F_{pix} = \frac{N_f}{\Phi_{pix}} = \frac{\gamma}{\Phi_{pix}\Delta\varphi} \tag{7}$$

With $\Delta\varphi$ from equation 1 and the two previous equations, this yields:

$$\frac{\Delta F_{pix}}{F_{pix}} = \frac{2\sqrt{Var_{F_{pix}}}}{F_{pix}} = \frac{2\sqrt{3}\lambda\alpha_{air}}{\pi D\gamma\sqrt{\Phi_{pix}SNR}} \tag{8}$$

Now, the presented uncertainty only considers the frequency estimate obtained from a single line in the out-focus disk. However, there is more information available to improve this estimate. The out-focus disk contains many lines from which an averaged frequency estimate can be calculated. Thus, when all the rows in a rectangular box enclosing the disk are averaged, this uncertainty has to be divided by the square root of the amount of rows Φ_{pix}. This yields:

$$\frac{\Delta F_{pix}}{F_{pix}} = \frac{2\sqrt{3}\lambda\alpha_{air}}{\pi D\gamma\Phi_{pix}\sqrt{SNR}} \tag{9}$$

$$= \frac{2\sqrt{3}}{\pi N_f\Phi_{pix}\sqrt{SNR}} \tag{10}$$

Two remarks on this important formula. First, note that this formula yields a slightly optimistic value. Averaging all rows of a disk, is not the same as averaging the frequency estimate of Φ_{pix} samples. The disk shape has the influence of a windowing function on the result. As demonstrated by So et al. (1999), windowing makes the periodogram slightly less accurate and therefore, this lower bound on the frequency estimate will not be obtained exactly. Nevertheless, it can still be used as a design guideline. The second remark concerns the use of compressing optics or rectangular apertures. For these cases, the uncertainty should be divided by the square root of the amount of rows in the out-focus image. While this value is per definition smaller than the horizontal size (to improve the concentration limit), the absence of windowing and the optical averaging involved will help to decrease the variance. As such, conclusions on the relative merits of the different configurations should be experimentally verified, which is beyond the scope of this article.

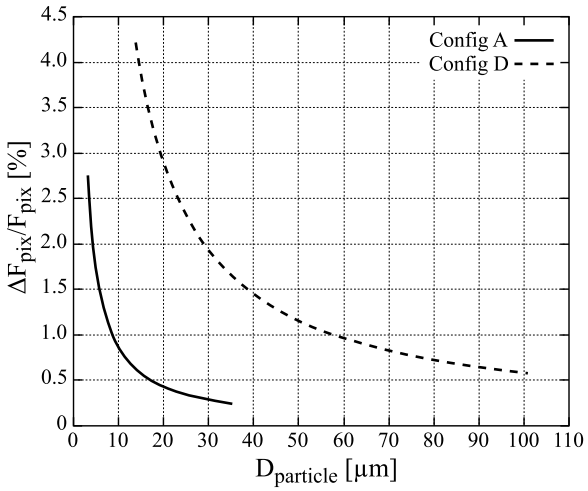

Figure 2 Uncertainty in frequency estimation versus particle diameter for two configurations proposed in Damaschke et al. (2002b).

Now, to obtain a better idea of the magnitude of this error, the procentual error is plotted versus the diameter of the particle in figure 2 for two of the example configurations that were theoretically proposed by Damaschke et al. (2002b) (configurations A and D). Configuration A is the reference case on which the influence of different parameters is tested and in configuration D, the influence of stand-off distance is demonstrated. For these configurations, a signal to noise ratio of 5 dB was assumed for a single row and the smallest particles. It is immediately apparent that larger particles are measured with a higher precision. Because the variance is independent of the absolute frequency, the procentual uncertainty decreases for larger frequencies; i.e. larger particle diameters. The absolute value of these errors is quite substantial; reaching up to 4% for configuration D. This is mainly caused by the very small number of pixels present in the out-focus disks; 22.5 for configuration A and 14.7 for configuration D. While these small values were chosen by the authors to obtain the highest possible concentrations, these results suggest that the price in precision should be considered as well. However, we do need to stress that the absolute errors obtained depend strongly on our choice of the signal-to-noise ratio.

As such, the best solution would be to have a design guideline that describes the necessary out-focus disk diameter in function of the SNR of the experiments or vice versa. To this end, the maximum error will be calculated analytically now. This error is obtained for the smallest diameter in the experiments or equivalently, the smallest amount of visible fringes. With $N_{f,min} = 1$ and a target maximum uncertainty of e.g. 1%, a suitable disk size can be chosen in function of the SNR of the measurements from equation 10. As an example, for a SNR of 5 dB, a minimum disk size of 62 pixels is needed. The other way around, configuration A would obtain a maximum

uncertainty of 1%, if SNR=14 dB, i.e. if the variance of the signal is 24 times larger than the variance of the noise in a single row.

Finally, we note that the SNR will also vary with the diameter of the particle. This is because the scattered light intensity varies with the square of the diameter while the background noise level is independent of this. On the other hand, a CCD camera integrates the light irradiance impacting on each pixel. Therefore, when the Nyquist criterion is reached and a single fringe covers only 2 pixels, most of the intensity variation will be averaged out, leading to a very small SNR as well. As a result, the dependency of SNR on the diameter becomes quite complicated and this is not taken into account in the previous formulas and the curves of figure 2. As a result, the uncertainty in the central portion of the diameter range is overpredicted slightly.

5 Uncertainty analysis of the calibration constant $C_{pix/rad}$

After the discussion of the uncertainties related to the conversion factor and the frequency estimation, the uncertainty of the calibration is next. Now, there exist several approaches to calculate $C_{pix/rad}$. These will be introduced in sections 5.1 to 5.4. In section 5.5, the two most used procedures will then be compared experimentally.

5.1 Fringe Counting

This is the oldest and also the easiest method for performing ILIDS measurements. It was already used by Ragucci et al. (1990). Note that in this approach there is no clear distinction between a measurement of the fringe spacing in pixels and a calibration of the amount of radian per pixel. Instead, only two variables need to be known, the collecting angle γ and the amount of fringes inside the ILIDS disk N_f. The collecting angle γ is equal to the total amount of radian that is gathered by the lens. Since this range of angles is mapped on the out-focus disk, one can calculate the angular fringe spacing by dividing the total amount of mapped radians by the total amount of fringes. Thus, we have:

$$\Delta\varphi = \frac{\gamma}{N_f} \tag{11}$$

The largest uncertainty associated with this measurement procedure is definitely due to the need to count the amount of fringes. By its very nature this is limited to integral numbers yielding an uncertainty of $\pm$ 1. In order to maintain an uncertainty percentage of 1%, the minimum amount of fringes in the disk should be 100. This reduces

the dynamic range and concentration limit of the technique significantly. In addition, when several disks overlap, a good measurement is likely to be impossible, reducing the allowable concentration even further.

5.2 Full Experimental Calibration

In this type of calibration, the mapping of radian to pixel is determined experimentally by fitting the obtained result to the known diameter of a calibration target. This was for instance done by Min and Gomez (1996). Depending on the calibration target this can be indeed a very accurate calibration.

Note however, that in this case one does not calibrate $C_{pix/rad}$ separately, but instead the product $\lambda\alpha_{air}F_{pix}C_{pix/rad}$. A positive consequence is the fact that small errors in α_{air} due to misalignment can be corrected in the calibration constant. A disadvantage is the possibility to introduce bias errors in the system. Any error in α_{air} during the calibration, e.g. due to overestimation of the refractive index, will end up in $C_{pix/rad}$. Now, even if the refractive index of the real measurement liquid is known perfectly, a bias error still exists.

A second difficulty of this approach is that it is very difficult to use this to calibrate ILIDS measurements on bubbles inside a closed reservoir. Apart from the difficulty of finding mono-disperse bubble generators, replicating the same configuration as found in the closed reservoir without changing the position of the camera or reservoir (to avoid bias errors) is very difficult.

5.3 Semi-Experimental Calibration

A much easier approach is the semi-experimental calibration. Here, the calibration value is obtained by dividing the out-focus disk size expressed in pixels by its size in radian. The disk size in radian is equal to the collecting angle γ, which, in our case, is obtained from a numerical ray-tracing calculation of the measured optical set-up. The disk size in pixel Φ_{pix} follows from locating the edges of the out-focus disk in the intensity profile. When the out-focus image is a disk, a Hough transform can be used as was done by Glover et al. (1995). This leads to the following formula:

$$C_{pix/rad} = \frac{\Phi_{pix}}{\gamma} \tag{12}$$

Note that this formula can be transformed into the formula for fringe counting since $F_{pix}\Phi_{pix}$ is simply equal to the total amount of fringes in the disk N_f! Thus, a fractional amount of fringes is obtained per particle. However, this does not mean that this approach is per definition more accurate than fringe counting since the uncertainty is

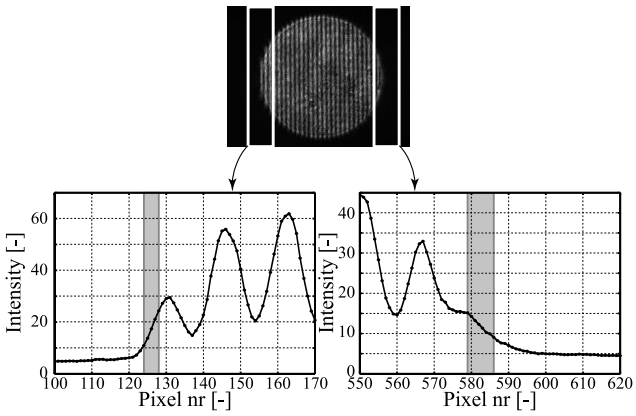

Figure 3 Illustration of the uncertainty in determining the out-focus disk size from an image

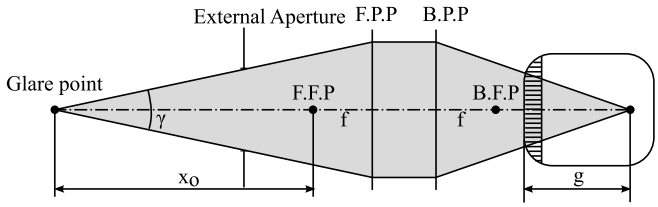

Figure 4 Thick lens approximation used to calculate the out-focus disk size theoretically

now spread over two terms. While section 4 showed that the uncertainty in the frequency determination with the Fourier Transform can be made quite small by using a large out-focus disk, nothing has been said so far to our knowledge concerning the uncertainty related to the disk size determination. In order to quantify this error, a sample intensity profile (averaged over all rows) is shown in Figure 3. As can be seen, the disk edge is not discontinuous but smoothed significantly by diffraction. This leads to a fundamental uncertainty concerning the correct location of the edge. In the present case, an uncertainty on the total disk size of 7 pixels must be allowed. This corresponds to an uncertainty of 1.5%. This value is by no means the average uncertainty but rather a lower bound as will be shown in Section 5.5 where the evolution of this value will be investigated for different parameters.

5.4 Theoretical Calibration

In Figure 3, one can already see on the zoom of the right edge that any computer program will have a very hard time to correctly detect the edge due to the fact that fringes continue to appear in the diffraction tails. Another problem which appears occasionally is the partial separation of the out-focus disks, resulting in similar oscillations in the edges. For this and other reasons it would be nice to calculate the expected disk size theoretically from the optical configuration. The traditional approach here is to use the thin lens approximation but this is not valid when using objectives (as the Micro-Nikkor 55mm lens in our experiments). Therefore, it is necessary to use the more

general thick lens approximations. For details of the thick lens approximation we refer to Hecht (1990). A simple derivation, based on the sketch of Figure 4, results in:

$$\Phi_{pix} = \frac{2\tan\left(\frac{\gamma}{2}\right) g x_o}{f S_{pix}} \tag{13}$$

Here, f is the focal length of the lens, g is the out-focus distance of the CCD-plane, x_o is the distance from the object to the front focal plane and S_{pix} is the size of a pixel. However, it is not the disk size that is needed, but the division of the disk size by the collecting angle. In this way, we obtain a term $2\tan\left(\frac{\gamma}{2}\right)/\gamma$. For moderate collecting angles, this term equals 1 since the error for a collecting angle of 10 is only 0.25%. Thus, the fringe spacing for the theoretical case is:

$$C_{pix/rad} = \frac{g x_o}{f S_{pix}} = \frac{g}{M S_{pix}} \tag{14}$$

where M is the in-focus magnification of the optical system. Note that the same formula has appeared based on the thin lens equations in Pan et al. (2005). Nevertheless, the fact that this calibration value does not depend on the collecting angle is a very important one! This implies that this configuration does not require an accurate size and position measurement of the aperture as opposed to the experimental calibration. Therefore, the internal aperture of the objective can be used. However, one of the important parameters in this case is g, the out-focus distance. While this can be measured in some configurations, it is not possible when an objective is used that is attached to the CCD-plane. Therefore, two special configurations will be introduced now which circumvent this problem elegantly.

5.4.1 Camera focused at infinity When the objective is focused at infinity, the exact position of the CCD-plane is known; i.e. at the back focal plane of the lens. This non-imaging configuration is quite similar to the one used by Koenig et al. (1986). This choice implies $g = x_i$ and this simplifies the theoretical formula to:

$$C_{pix/rad} = \frac{f}{S_{pix}} \tag{15}$$

which is an amazingly simple formula. Note that in this case, there is even no need to measure the location of the camera x_o! Aside from its practical ease this also implies that there are almost no uncertainties left in this case. Both the focal length and the pixel size are values supplied by the vendor. While this configuration only allows the measurement of one particle at a time, it could be useful when a very high precision is required.

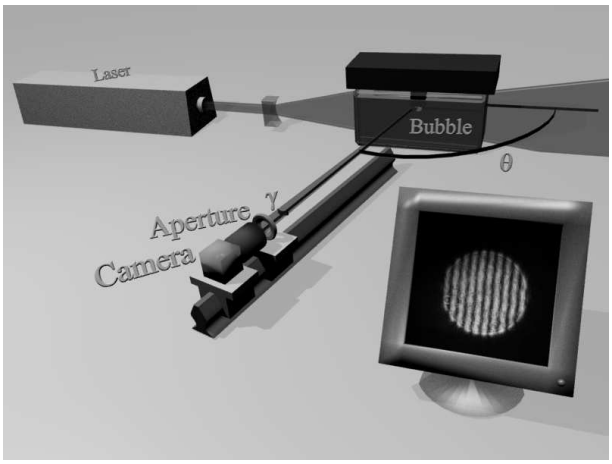

Figure 5 Experimental configuration to obtain a stable bubble

5.4.2 Two-step theoretical calibration A second possibility to use with commercial objectives is the two-step calibration as introduced in Pan et al. (2005). In a first step, the camera is focused at the target. Here, the distance $x_{o,if}$, being the distance from the front focal plane to the measurement volume, or the in-focus optical magnification M_{if} is measured. Then, the entire camera (CCD + objective) is displaced by an accurately measured amount h. This results in the following formula:

$$C_{pix/rad} = \frac{fh}{x_{o,if} S_{pix}} = \frac{M_{if} h}{S_{pix}} \tag{16}$$

5.5 Comparison of experimental and theoretical calibration

5.5.1 Experimental Set-Up In order to quantify the errors related to the semi-experimental and theoretical calibration procedure, two sets of experiments were performed. To this end, it was necessary to have a stable bubble on which different configurations could be tested sequentially. This was achieved with the configuration shown in figure 5. A reservoir filled with silicone oil (n=1.403) is used and the bubble is simply kept immersed by a wooden obstruction. Naturally, this leads to some non-sphericity in the vertical plane. However, as ILIDS measures the diameter of the bubble in a horizontal plane and all forces in this plane are symmetrical, the bubble is spherical as far as ILIDS is concerned.

5.5.2 Camera focused at infinity In order to test the theory, the theoretical disk size was calculated and compared with the experimentally measured disk size for different positions of the camera along the rail in figure 5. The result of this comparison is shown in figure 6(a). While the correct trend is obviously captured by the theoretical continuous line, there is a substantial bias towards larger disk sizes. Analysis of this bias shows that the error is around 2%

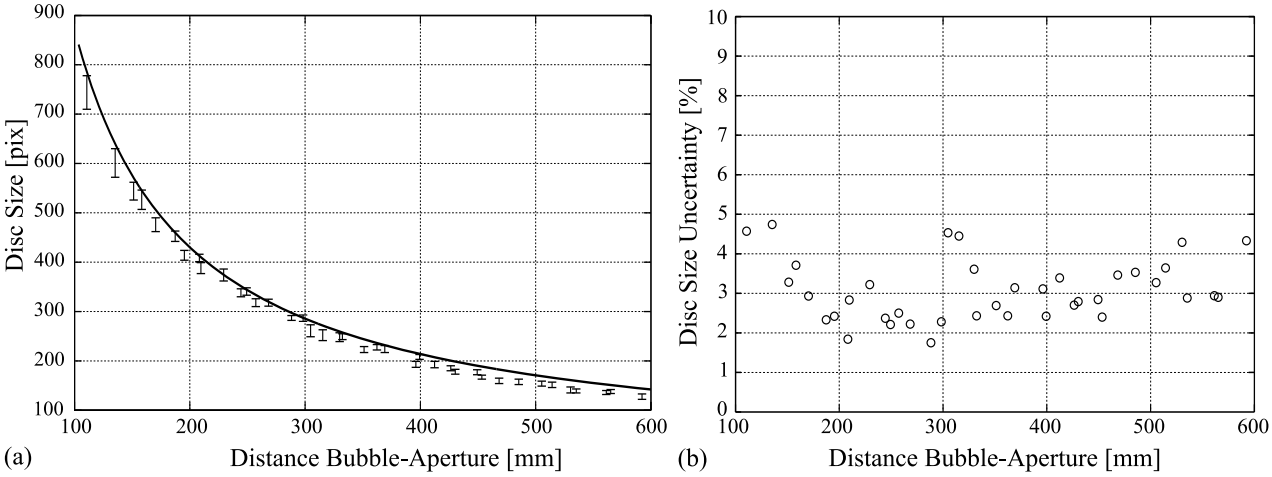

Figure 6 (a) Experimental versus theoretical disk size for a camera focused at infinity (b) Experimental uncertainty of the disk size determination

for the smallest stand-off distance and increases linearly up to 12% for larger distances. Since the uncertainty on the experimental disk size determination is approximately constant at 3% (figure 6(b)), the error must come from the theoretical disk size calculation. In order to pinpoint the culprit, a sensitivity analysis was performed of the theoretical formula. This showed that an error of this magnitude could not be attributed to incorrect measurements of the collecting angle (which still plays a role in the theoretical *disk size* calculation). Additionally, a separate measurement of the focal length of the objective gave a result of 54.8 mm, which only introduces a constant bias of 0.4%. Finally, it was found that both the trend as the magnitude of the bias could be explained by assuming that the CCD-plane is shifted by *only 0.5 mm* from the back focal plane! This can be appreciated from the theoretical disk size formula of section 5.4. In this case, there will be a constant error Δg. Since g decreases as the objective is placed further from the bubble, the procentual error $\frac{\Delta g}{g}$ will increase with distance as was observed in the experiment. This clearly shows that the theoretical configuration is extremely sensitive for this configuration, since a misplacement of 0.5 mm already results in errors of up to 12%.

Concerning the experimental calibration, we repeat that the uncertainty is approximately constant, independent of total disk size and stand-off distance. The average uncertainty was found to be close to 3%. This uncertainty was calculated as follows. First, the intensity and position where the interference pattern is thought to be 'lost' and the diffraction tail begins is manually located. Starting from the local background intensity, the real edge is assumed to lie between those locations where the intensity in the diffraction tail breaches 0.25 and 0.75 times the gap in intensity between signal and background. Note that, while these values might seem random, there are at present no

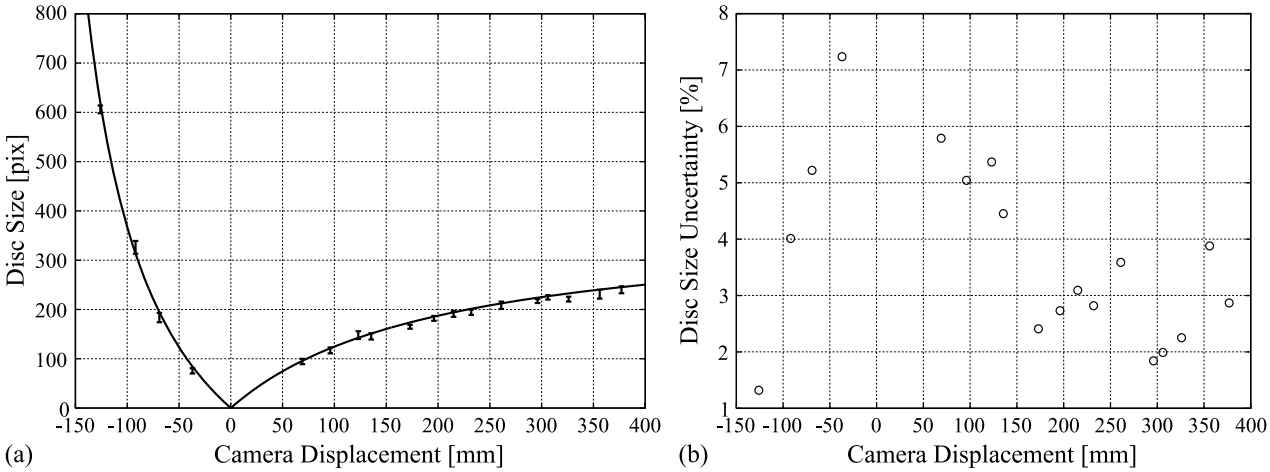

Figure 7 (a) Comparison of theoretical and experimental disk sizes for the two-step calibration procedure in function of the camera displacement h from the focus position (b) Experimental uncertainty of the disk size determination

theoretical predictions available that can narrow this search field in our opinion. To this uncertainty, one needs to add the uncertainty on the collecting angle ($\leq 1\%$) in order to obtain the total calibration uncertainty of 3%.

5.5.3 Two-step calibration One of the basic flaws of the previous configuration for a successful theoretical calibration was the decreasing out-focus distance as the camera is placed further away. The inverse approach however should result in decreasing uncertainties. This can be achieved by focusing the camera not at infinity but at its closest possible focus. A theoretical calibration in this case must follow the two-step procedure explained earlier. Again, the two procedures were experimentally verified by comparing the theoretical and experimental disk sizes for different camera displacements h as shown in Figure 7a. Naturally, the disk size tends to zero when $h = 0$, i.e. the bubble is in-focus. From this point, it increases going closer to (negative h) or further away from (positive h) the bubble with the camera. Note that, while not apparent from the graph, negative values of h were unsuited for ILIDS measurements since the disks did not overlap completely. From the comparison, we see that, with this calibration technique, the theoretical and experimental results were in agreement.

Finally, concerning the uncertainty on the disk size determination; this reaches a peak close to the focusing position and decreases going further. However, when h approaches 300 the uncertainty stops decreasing and appears to remain constant afterwards at around 3% again.

6 Discussion

6.1 Calibration tips

Counting fringes is by far the most inaccurate procedure to measure the diameter due to the impossibility to count accurately a fractional amount of fringes. This can be improved by performing an FFT-analysis but this has to be combined with a calibration of the amount of pixels per radian. As a general rule, one can say that the uncertainty on the semi-experimental calibration is around 3% mostly due to diffraction effects and the ambiguity in locating the 'real' edge location. However, no experiments were performed with different objectives and different aperture locations and shapes so this value cannot be taken as a universal constraint on the precision of the semi-experimental calibration procedure. A theoretical calibration can yield an improved calibration when the objective is focused on its closest point. With the described two-step calibration procedure, the main error sources are the determination of the in-focus optical magnification and the out-focus displacement of the entire camera h. In the present experiment, we obtained a variation of the magnification across the laser-sheet thickness of 0.6%. In addition, when measuring at $h = 400$ mm with an estimated uncertainty on h of 1 mm, one needs to add a procentual uncertainty of 0.25%. This leads to a combined uncertainty on the calibration of 0.7%, which is a huge improvement over the experimental calibration. However, this could have been improved even more by considering the fact that the uncertainty on the in-focus magnification is really just due to the variation in $x_{o,if}$ across the laser-sheet thickness. Assuming for simplicity that $\Delta x_{o,if} = \Delta h$, this leads to an optimal configuration when $x_{o,if} = h$ since both uncertainties are equal then. Thus, for a given stand-off distance of the camera, the highest precision is obtained when the camera reaches a sharp focus half-way to the measurement volume. In cases where the precision in h is higher than in $x_{o,if}$, the in-focus position is further away from the particle.

However, these types of 'static' calibration, where the conversion is calculated before the measurements start, are not possible in cases where the disk size varies significantly for different positions in the laser-sheet. This is for example the case when one attempts to measure the third velocity component from the disk size. In this case, a combined theoretical and experimental procedure as performed by Grassmann and Peters (2004) can be used. Here, one first measures the disk size in pixels experimentally. This disk size is then placed in the theoretical disk size formulas to obtain the missing parameters as x_o, θ and γ. However, in this way, the uncertainty in the disk size determination can propagate to other parameters, possibly reducing the overall precision significantly.

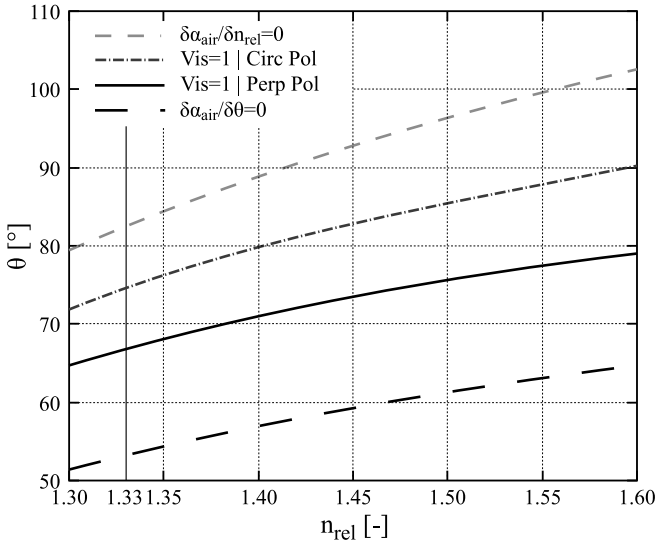

Figure 8 Special angles for ILIDS measurements on droplets where observation angle, refractive index and frequency determination uncertainties are minimal

6.2 Designing a maximum precision ILIDS configuration for droplets

Damaschke et al. (2002b) already provided several design guidelines for measurements on droplets. However, they did not discuss the influence of the observation angle, nor the precision constraints that should drive the choice of the out-focus disk size.

The influence of the observation angle is present in the conversion factor α_{air}. In section 3, we mentioned that there exists a special angle that minimizes this dependency. The precise angle where this minimum is obtained depends on the relative refractive index of the droplet. Its evolution is shown in the bottom curve in figure 8. The top curve represents the limiting angle for refraction. All observation angles above this have no dependency on the relative refractive index. Finally, the two central curves correspond to the angles that yield a visibility of 1. This is defined as: $Vis = (I_{max} - I_{min}) \,/\, (I_{max} + I_{min})$ and reaches a maximum value of 1 when both glare points are equally intense. For perpendicular and circular polarized light, the angle where this ideal situation is reached can be calculated with traditional geometrical optics. In order to calculate the best configuration for parallel polarized light, surface waves must be taken in consideration. Since this is not possible with our code, this result will not be shown. Now, the importance of these visibility lines is that they lead to a larger SNR. Since a larger SNR leads to lower frequency estimate errors, measuring close to these lines will minimize this particular uncertainty.

With the help of this graph, we are now ready to formulate some design guidelines;

Observation angle: The best approach here is to estimate in advance the uncertainties on the observation angle and relative refractive index. Then choose an observation angle, in accordance with figure 1, to equalize both expected errors and only then choose the polarization that will yield the maximum visibility from figure 8.

Collecting angle: The primary influence of the collecting angle is setting the minimum measurable diameter. Therefore, this is chosen from the equation $\gamma = \lambda\alpha_{air}/D_{min}$

Stand-off distance: Using the largest possible aperture, a maximum stand-off distance of the camera to the spray is obtained. This helps in minimizing observation angle changes across the field of view and general misalignment errors. Calibration errors will also be smaller due to the smaller procentual uncertainty in the determination of the collecting angle or $x_{o,if}$ from the geometric configuration of the set-up.

Out-focus disk size: There are three constraints on Φ_{pix}. The first one is its influence on the maximum measurable diameter because $D_{max} = \lambda\alpha_{air}\Phi_{pix}/2\gamma$. The second is the influence on the frequency estimation accuracy (equation 10). Finally, the disk size is also determined by the choice of the focal length of the optics and the CCD-plane position. As mentioned in the previous subsection, reaching a sharp focus half-way the measurement volume would reduce the calibration error. With $h = x_{o,if}$, the third constraint is: $\Phi_{pix} = \gamma f/S_{pix}$. From these constraints, the first one denotes the absolute minimum out-focus diameter since the maximum measurable diameter is fixed by the experiment. When only one or both of the other constraints indicate larger diameters, the choice, once again should be guided by obtaining the smallest overall uncertainty from the formulas 10 and the combination of 13 and 16 based on the estimated uncertainties in the parameters. The real problem off course is the need for an estimate of the SNR but this can be obtained from preliminary test results.

Focal length, CCD-plane position: These parameters follow from the choice of out-focus disk size and the minimization of the calibration error.

Once all of the above parameters are found, the maximum obtainable concentration can then be found following Damaschke et al. (2002b).

A small example; we want to measure water droplets ($n_{rel} = 1.33 \pm 0.01$, $D_{min} = 100\mu m$, $D_{max} = 500\mu m$) with an objective with a fixed focal length of 55 mm and an external aperture of 1 cm. The expected uncertainty in the observation angle determination is 1° and on $x_{o,if}$ and h is 5 mm. Now, the observation angle and refractive index errors are balanced close to 60° ($\pm 0.1\%$). This angle is to be used with perpendicular polarization to obtain the best visibility. A collecting angle of 0.34° is needed to measure the smallest droplets, which leads to a maximum stand-off distance of 1.73 m. The three constraints on the out-focus disk size lead to 10, 62 and 49

pixels respectively. Since the calibration errors in this case only add up to 0.8% and the FFT-error equals 1% for the smallest diameter (SNR=5dB), one should use an out-focus disk size of 62 pixels. This should be obtained by decreasing $x_{o,if}$ a little bit, thus increasing h and Φ_{pix}. Fortunately, the calibration error in this case is still below the FFT error with a value of 0.9%. Thus, a total uncertainty of 1.3% is obtained! Note that a slightly smaller uncertainty could be obtained by increasing the out-focus disk size to the point where calibration and FFT errors are equal. Another approach would be to maximize the SNR by choosing an observation angle of 68°. This would decrease the main error source, the frequency error, and smaller overall errors would be obtained.

7 Conclusions

A thorough study of the different uncertainty sources for measuring particles with ILIDS was conducted. The influence of non-sphericity on the measurements was shown to broaden the obtained diameter distribution while keeping the mean approximately constant. Next to this, an analytic analysis of the precision of the frequency estimate was performed for the first time. This yielded the first design guidelines on the necessary out-focus disk size in function of the signal to noise ratio of the experiments. Then, the uncertainty of different calibration procedures was experimentally tested. This showed that a theoretical calibration, based on the thick lens formulas gives the best results. This also showed that the highest precision is obtained when the camera reaches its focusing position roughly midway the camera's final position. In conclusion, design guidelines were assembled for minimizing the combined uncertainty on the measurements. This showed that, for ILIDS measurements on droplets, the main error sources are the calibration and the frequency estimation. Nevertheless, combined uncertainties below 1.5% are realistic.

Acknowledgments

We would like to thank R. Prete for the help during our experiments. This research was funded with fellowship SB-031241 granted by the Institute for the Promotion of Innovation through Science and Technology in Flanders (IWT-Vlaanderen).

References

H.-E. Albrecht, M. Borys, N. Damaschke, and C. Tropea. *Laser Doppler and Phase Doppler Measurement Techniques*. Springer-Verlag, 2003.

J. Burke, C. Hess, and V. Kebbel. Digital holography for whole field spray diagnostics. In *11th International Symposium on Application of Laser Techniques to Fluid Mechanics*, Lisbon, 2002.

N. Damaschke, H. Nobach, T.I. Nonn, N. Semidetnov, and C. Tropea. Size and Velocity Measurements with the Global Phase Doppler Technique. In *11th international symposium on application of laser techniques to fluid mechanics*, Lisbon, 2002a.

N. Damaschke, H. Nobach, and C. Tropea. Optical limits of particle concentration for multi-dimensional particle sizing techniques in fluid mechanics. *Experiments in Fluids*, 32:143–152, 2002b.

S. Dehaeck and J.P.A.J. van Beeck. Demonstration and characterisation of a new interferometric particle imaging configuration for bubbles. In *13th Int Symp on Applications of Laser Techniques to Fluid Mechanics*, 2006.

S. Dehaeck, J.P.A.J. van Beeck, and M.L. Riethmuller. Glare Point Velocimetry and Sizing (GPVS): Introduction of a new optical 2D measuring technique for bubbly flows. In *12th International Symposium on Application of Laser Techniques to Fluid Mechanics*, Lisbon, 2004.

S. Dehaeck, J.P.A.J. van Beeck, and M.L. Riethmuller. Extended glare point velocimetry and sizing for bubbly flows. *Experiments in fluids*, 39(2):10.1007/s00348-005-1004-6, August 2005.

A.R. Glover, S.M. Skippon, and R.D. Boyle. Interferometric laser imaging for droplet sizing: a method for droplet-size measurement in sparse spray systems. *Applied Optics*, 34:8409–8421, 1995.

A. Grassmann and F. Peters. Size measurement of very small spherical particles by mie scattering imaging (msi). *Part. Part. Syst. Charact.*, 21:379–389, 2004.

Hecht. *Optics*. Addison Wesley, 1990.

C.F. Hess. Planar particle image analyzer. In *9th International Symposium on Applications of Laser Techniques to Fluid Mechanics*, Lisbon, 1998.

G. Koenig, K. Anders, and A. Frohn. A new light-scattering technique to measure the diameter of periodically generated moving droplets. *Journal of Aerosol Sciences*, 17:157–167, 1986.

M. Maeda, T. Kawaguchi, and K. Hishida. Novel interferometric measurement of size and velocity distributions of spherical particles in fluid flows. *Meas. Sci. Technol.*, 11:L13–L18, 2000.

P. Massoli and R. Calabria. Sizing of droplets in reactive sprays by mie scattering imaging. In *15th conference on liquid atomization and spray systems*, 1999.

S. L. Min and A. Gomez. High-resolution size measurement of single spherical particles with a fast fourier transform of the angular scattering intensity. *Applied Optics*, 35(24):4919–4926, 1996.

G. Pan, J. Shakal, W. Lai, R. Calabria, and P. Massoli. Simultaneous global size and velocity measurement of droplets and sprays. In *Proceedings of the 20th ILASS - Europe Meeting*, 2005.

R. Ragucci, A. Cavaliere, and P. Massoli. Drop sizing by laser light scattering exploiting intensity angular oscillation in the mie regime. *Part. Part. Syst. Charact.*, 7:221–225, 1990.

N. Semidetnov and C. Tropea. Conversion relationships for multidimensional particle sizing techniques. *Measurement Science and Technology*, 15:112–118, 2004.

H. C. So, Y. T. Chan, Q. Ma, and P. C. Ching. Comparison of various periodograms for sinusoid detection and frequency estimation. *IEEE Transactions on aerospace and electronic systems*, 35(3):945–952, July 1999.

H.C. So and Y.T. Chan. Short-time frequency estimation of a real sinusoid. *IEICE Trans. Fundamentals*, E88-A: 2455–2459, 2005.